RSC Advances

PAPER

View Article Online
View Journal | View Issue

Cite this: *RSC Adv.*, 2026, **16**, 1

Atomic perspective elucidates mixed alcohol synthesis from syngas on bilayered (K)/MoS_2 catalysts

Yaru Dang,[a] Qianji Han, *[a] Ruihan Wang, [a] Ziyan Wei,[a] Meng Wang[b] and Bin Qin*[c]

Syngas serves as a crucial link between non-petroleum-based carbon resources and commodity chemicals. Among various conversion routes, the catalytic transformation of syngas into ethanol and other mixed alcohols represents a highly attractive option. K-modified MoS_2 systems exhibit notable activity and selectivity in low-carbon alcohol synthesis. To elucidate the correlation between product selectivity and catalyst structure, and to design efficient catalysts for the synthesis of specific single products, density functional theory (DFT) was employed to explore the transition states of elementary steps involved in syngas conversion to mixed alcohols on bilayer (K)/MoS_2 catalysts. The results indicate that CO hydrogenation on the S-edge sites of the MoS_2(100) facet mainly yields C_1 species, whereas ethanol is primarily produced at the Mo-edge sites. Moreover, K doping enhances CO activation and C–C coupling at the Mo-edge. The most favorable pathway for ethanol synthesis at the Mo-edge is identified as CO → HCO → CHOH → CH → CHCO → CH_2CO → CH_3CO → CH_3CHO → CH_3CH_2O → CH_3CH_2OH, with the key step being the hydrogenation of CH_3CO to CH_3CHO, which requires an energy barrier of 0.73 eV. This work offers comprehensive and valuable guidance for the subsequent modification and design of C–C coupling catalysts.

Received 17th November 2025
Accepted 16th December 2025

DOI: 10.1039/d5ra08871b

rsc.li/rsc-advances

Introduction

The conversion of syngas to C_{2+} oxygenates has drawn significant attention in catalysis, as it provides a promising route for producing fuels and chemicals from non-petroleum resources such as coal, natural gas, and biomass.[1–5] Ethanol, one of the most important C_{2+} oxygenates, has been extensively applied in medical and energy sectors.[6] Conventionally, ethanol is obtained through grain fermentation, which inevitably competes with food supply for human consumption.[7,8] Direct ethanol synthesis from syngas over a single catalyst has been widely investigated, with studies focusing on rhodium-based catalysts, molybdenum-based catalysts, bi- or multi-component catalysts, modified Fischer–Tropsch catalysts, and modified methanol synthesis catalysts.[9–12] However, the reported catalysts still exhibit limited performance in practical applications. The major challenge lies in achieving high ethanol selectivity, which requires precise control of C–C coupling between intermediate CO dissociative and non-dissociative activated species.[13,14] In most cases, several elementary reactions occur simultaneously, inevitably resulting in multiple parallel pathways and a broadened product distribution.[9,15] Developing catalytic system that can steer the reaction toward a single dominant pathway is therefore essential for selective ethanol production from syngas.

In recent years, numerous heterogeneous catalysts have been investigated for the conversion of syngas to mixed alcohols. Among the five representative catalyst types for producing low-carbon alcohols from syngas, molybdenum sulfide-based catalysts have received considerable attention owing to their inherent resistance to carbon and sulfur poisoning. However, current MoS_2-based catalysts suffer from low activity and limited alcohol selectivity. The selectivity can be shifted from hydrocarbons toward alcohols by introducing suitable promoters, such as alkali metals, and by applying alternative reaction conditions.[16–19] Ao M. *et al.*[20] demonstrated that the key factors influencing MoS_2-based catalysts include the role of alkali metals (*e.g.*, Li, Na, K, and Rb), Fischer–Tropsch elements (*e.g.*, Fe, Co, and Ni), noble metals (*e.g.*, Rh and Pd), as well as the nature of the support. A review by Luk H. T. and co-workers on the status and prospects of advanced alcohol synthesis from syngas highlighted the ten most effective Mo-based catalysts.[9] According to their data, the K- and Ni-modified MoS_2 systems exhibit high activity and selectivity for higher alcohols (HA) synthesis, which is of great significance for research. Zhao *et al.*[21] synthesized KNiMo-based catalysts using four different

[a]*Chemical Engineering College, Hebei Normal University of Science & Technology, Qinhuangdao, Hebei 066600, PR China. E-mail: hanqianji4193@hevttc.edu.cn*

[b]*Department of Ecology, Hebei University of Environmental Engineering, Qinhuangdao, 0666102, China*

[c]*Key Laboratory of Advanced Energy Materials Chemistry of Ministry of Education, College of Chemistry, Nankai University, Tianjin 300071, China. E-mail: qinbin@nankai.edu.cn*

methods, and found that the non-thermal plasma route produced thinner and shorter MoS_2 plates, exposed more unsaturated sites, and increased in the number of active centers for alcohol formation. Compared with catalysts prepared by conventional thermal methods, these catalysts displayed higher dispersion and coordination unsaturation, resulting in superior catalytic performance. Consistently, Claure *et al.*[22] reported similar findings.

Experimental investigations aimed at correlating product selectivity with catalyst structure in syngas conversion remain highly challenging.[23] Therefore, elucidating the catalytic mechanism of syngas conversion is essential for the rational regulation of product selectivity. In recent years, density functional theory (DFT) has been increasingly employed to gain qualitative insights into catalytic surfaces.[24] However, the nature of the active sites and the detailed reaction mechanism on MoS_2 catalysts are still under debate. During the conversion of syngas to ethanol, CO is first hydrogenated to generate formyl species, followed by further hydrogenation and CO insertion. Previous studies have demonstrated that CO can be inserted into CH_x species to form CH_xCO on MoS_2 catalysts.[25,26] Meanwhile, the reaction pathways of ethanol formation from syngas have also been investigated. It has been reported that OCCHO species act as key intermediates in ethanol synthesis on the Cu(211) surface[27] and Cu/ZnO catalyst.[28] Wang *et al.*[29] reported that the catalytic effect of Cu-modified MoS_2 catalyst on the formation of ethanol is mainly manifested in the fact that Cu provided undissociated CHO, and the reaction of CH_2 inserted into CHO to form CH_2CHO also occurred at the boundary of the Cu_4 and MoS_2. Thus, the synergistic interaction between Cu and MoS_2 promotes the incorporation of CHO into CH_2. A clearer understanding of these fundamental aspects will facilitate the identification of active sites on MoS_2 catalysts and accelerate the rational design and development of advanced catalysts for CO hydrogenation.

The catalytic mechanism of alcohol synthesis from syngas has been investigated for decades, yet it remains unclear due to its inherent complexity.[30] In this study, Density Functional Theory (DFT) calculations were employed to examine the influence of alkali promoters on CO activation, CH_x species formation, C–C coupling, and hydrogenation of C_2 intermediates over MoS_2 catalysts. Although several theoretical studies have addressed alkali-promoted MoS_2 catalysts for syngas conversion, only a few have provided a more comprehensive reaction network for ethanol synthesis on bilayer molybdenum sulfide nanosheets. The insights obtained in this study are expected to contribute to the rational design of future catalysts.

Computational methods

Plane-wave DFT calculations employing the projector-augmented wave (PAW) method[31] were performed using the Vienna *ab initio* simulation package (VASP).[32,33] The generalized gradient approximation (GGA) with the Perdew–Burke–Ernzerhof (PBE) functional[34] was adopted for all computations, with a plane-wave cutoff energy of 400 eV. van der Waals (vdW) interactions were included using Grimme's DFT-D3 scheme.[35] Geometry optimization was carried out until the residual forces were smaller than 0.05 eV $Å^{-1}$ and the total energy difference was below 10^{-4} eV. A Monkhorst–Pack[36] *k*-point mesh of $(2 \times 1 \times 1)$ was applied for Brillouin zone sampling.

The bulk MoS_2 structure was obtained through full energy minimization of both lattice vectors and atomic coordinates. The $MoS_2(100)$ surface was modeled as a $p(3 \times 3)$ periodic slab containing 7 atomic layers. Based on these considerations, a double-layer $MoS_2(100)$ slab was constructed with a 15 Å vacuum gap along both the *b* and *c* directions, which better represents nanosheet catalysts observed in experiments.

To determine the energy barriers, transition states (TS) were identified using the nudged elastic band (NEB) method.[37] The TS structures were confirmed by harmonic vibrational frequency analysis of the adsorbates, where only one imaginary mode was detected. Charge density difference analysis and Electron Localization Function (ELF) analysis was performed using the VESTA program.[38] The charge difference before and after the adsorption of an adsorbate: $\Delta\rho = \rho(\text{slab} + \text{ads}) - \rho(\text{ads}) - \rho(\text{slab})$.

All structures were built and visualized using Materials Visualizer from Materials Studio. The activation barrier (E_a) and reaction energy ($\Delta_r E$) were evaluated as $E_a = E_{TS} - E_{IS}$ and $\Delta_r E = E_{FS} - E_{IS}$, where E_{IS}, E_{FS}, and E_{TS} denote the energies of the initial state (IS), final state (FS), and transition state (TS), respectively.

Differential charge density and projected density of states analyses were performed using the DS-PAW package.[39] *Ab initio* molecular dynamics (AIMD) simulations were performed using the VASP code. The *NVT* ensemble with the Nosé–Hoover thermostat[40,41] was employed with a time step of 1 fs at the typical reaction temperature of 600 K.

Results and discussion

Bulk and surface structures

MoS_2 belongs to a class of materials known as layered compounds and exists in three polymorphic modifications: 1T, 3R, and 2H, with the latter being the most stable.[42] In bulk MoS_2, each Mo atom is coordinated by six S atoms in a trigonal prismatic arrangement (Fig. 1). For the optimized bulk model, a stable 2H-MoS_2 primitive cell belonging to the $P6_3/mmc$ space group was employed. The calculated lattice constants of bulk MoS_2 are $a = b = 3.18$ Å and $c = 13.39$ Å, which are consistent with the experimental value of 3.20 Å.[43] The S–Mo–S bond angle is 80.95°, and the Mo–S bond length is 2.41 Å. The optimized bilayer MoS_2 structure is presented in Fig. 1, with an interlayer spacing of 6.71 Å.

For the MoS_2 surface model, two types of bilayer-stacked (100) planes were conducted, resulting in a Mo-terminated edge and an S-terminated edge, in accordance with the widely accepted "Rim-Edge" model.[40] On the Mo_0–S_{100} surface, half of the surface S atoms from the S-terminated edge were transferred to the Mo-terminated edge, producing a configuration with 50% S concentration at both edges, defined as the Mo_{50}–S_{50} surface. Previous DFT calculations demonstrated that the Mo_{50}–S_{50} surface exhibits the highest energetic stability under

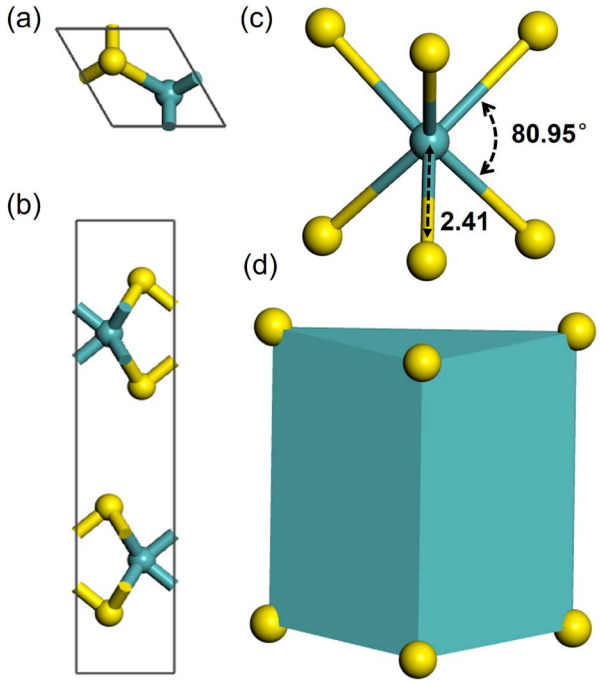

Fig. 1 The optimized bulk crystal structure of 2H-MoS_2: (a) top-view; (b) side-view; (c) the constructing unit of 2H-MoS_2 (bond lengths in Å); (d) the corresponding polyhedron of 2H-MoS_2. The cyan and yellow spheres represent the Mo and S atom, respectively.

Table 1 Calculated Bader charge for MoS_2(100) and K/MoS_2(100) surfaces

Element symbol	Label	MoS_2(100)	K/MoS_2(100)
Mo	63	1.24	1.17
Mo	66	1.25	1.16
Mo	69	1.14	1.17
Mo	72	1.15	1.20
Mo	51	1.02	1.02
Mo	54	1.03	1.03
Mo	57	1.02	1.03
Mo	60	1.02	1.03
S	3	−0.51	−0.65
S	12	−0.50	−0.64
S	15	−0.48	−0.53
S	24	−0.49	−0.54
S	6	−0.61	−0.63
S	9	−0.60	−0.74
S	18	−0.61	−0.63
S	21	−0.60	−0.60
K	73	—	0.87

hydrodesulfurization (HDS) conditions.[44] Under the sulfo-reductive atmosphere used for CO hydrogenation, the catalytic system is exposed to a relatively low sulfur chemical potential. According to earlier DFT studies, this environment stabilizes a sulfur coverage of 37.5% at the Mo-edge of MoS_2, corresponding to 3 S atoms per 4 Mo-edge atoms in the supercell.[45] By removing one S atom from the Mo-edge of the Mo_{50}–S_{50} surface, a model with 37.5% sulfur coverage at the Mo-edge and 50% sulfur coverage at the S-edge was obtained, hereafter denoted as the $Mo_{37.5}$–S_{50} surface (Fig. 2a). Furthermore, to clarify the role of the K promoter in syngas conversion to ethanol, a K-doped structure was also considered, referred to as K/$Mo_{37.5}$–S_{50}.

The electronic distribution of the $Mo_{37.5}$–S_{50} model was visualized using the Electron Localization Function (ELF): in the 2D cross-sectional heat map (Fig. 2b), the color scale from red to blue represents the variation of electron localization from strong to weak. Combined with its layered crystal structure, the green isosurfaces correspond to highly localized electron regions (such as strong intralayer covalent Mo–S bonds or lone pairs). This electronic distribution directly determines its catalytic properties: the edge sites of MoS_2 layers, due to unsaturated coordination, exhibit tuned electron localization

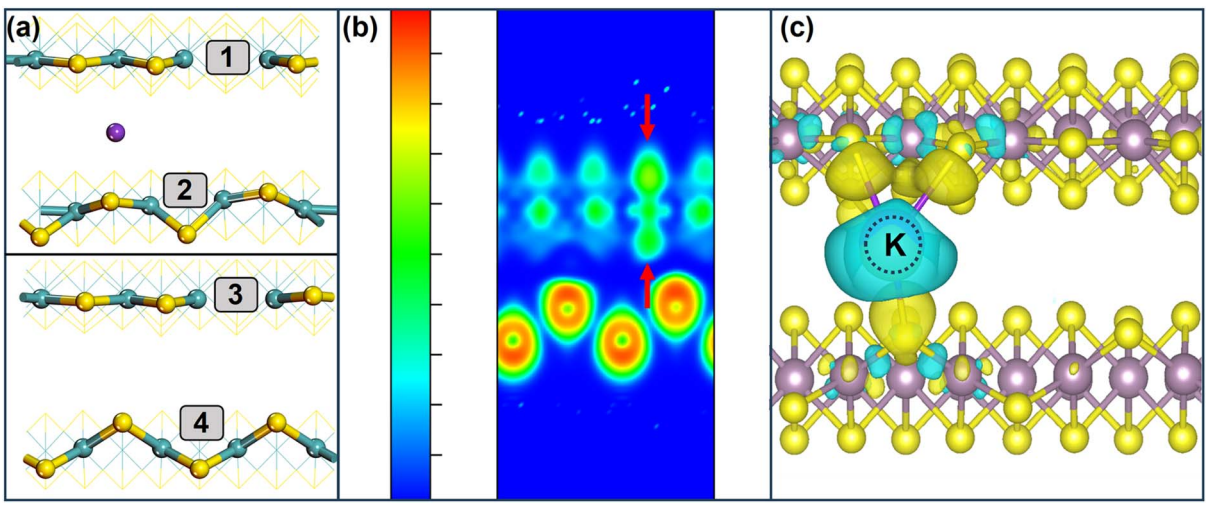

Fig. 2 (a) The optimized structure of reaction sites: (1) Mo@K/MoS_2(100); (2) S@K/MoS_2(100); (3) Mo@MoS_2(100); (4) S@MoS_2(100); (b) top view and side view of the electron localization function (ELF) for $Mo_{37.5}$–S_{50} model; (c) differential charge density of K/$Mo_{37.5}$–S_{50} model (yellow represents electron accumulation; equivalence plane: 0.03 e bohr^{-3}).

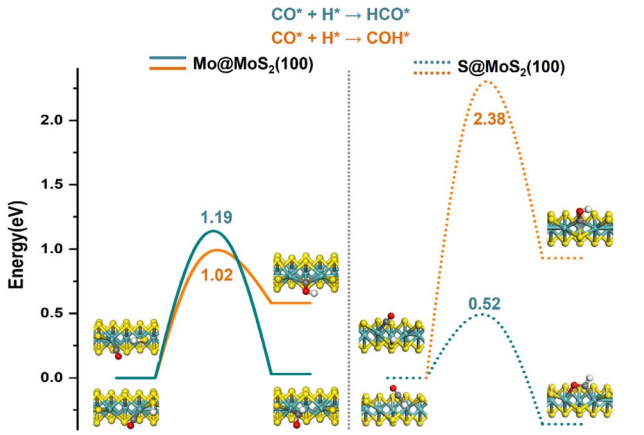

Fig. 3 Schematic structure of the CO activation process on the Mo@MoS_2(100) site and S@MoS_2(100) site.

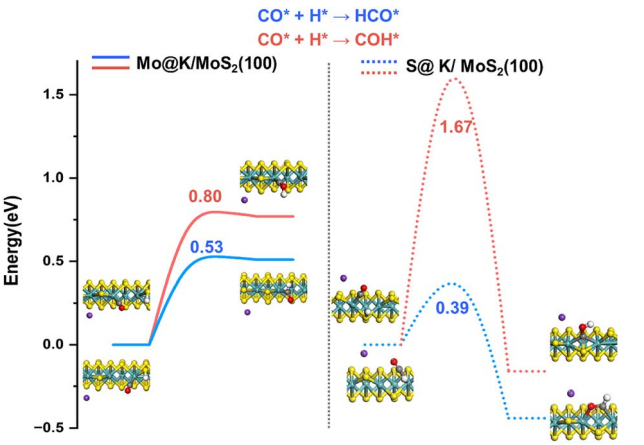

Fig. 4 Schematic structure of the CO activation process on the Mo@K/MoS_2(100) site and S@K/MoS_2(100) site.

and serve as the primary active centers for hydrogenation reactions. Defects such as sulfur vacancies can reconstruct the local electronic structure to enhance intermediate adsorption. Regions with low electron localization facilitate electron transfer during catalytic reactions. Notably, at the S vacancies on the Mo-edge of this model, a significant accumulation of Mo d_{z^2} electrons can be observed, making this site more receptive to reactants from both directions. However, due to the limited interlayer distance, reactants are more likely to approach this site from the outer side, thereby enhancing the activation capability of the edge and corner sites.

On the $Mo_{37.5}$–S_{50} surface, the most stable site for K adsorption is an interstitial position coordinated with three S atoms, as shown in Fig. 2c. In this configuration, K forms threefold coordination with two surface S atoms at the Mo-edge and one surface S atom at the S-edge. The differential charge analysis indicates that the K atom donates electrons to both the Mo-edge and the S-edge. Consequently, the adsorbed K atom alters the interstitial region of the (100) edge surface. As a result, four distinct types of reaction sites can be distinguished, as illustrated in Fig. 2a. The first site corresponds to an unsaturated coordination site (CUS) at the Mo-edge of the K/$Mo_{37.5}$–S_{50} model, designated as the Mo@K/MoS_2(100) site. The second site is a Mo–Mo bridge located at the S-edge of the K/$Mo_{37.5}$–S_{50} model, denoted as the S@K/MoS_2(100) site. The third site is another CUS, but located at the Mo-edge of the $Mo_{37.5}$–S_{50} model, referred to as the Mo@MoS_2(100) site. Finally, the fourth site corresponds to a Mo–Mo bridge on the S-edge of the $Mo_{37.5}$–S_{50} model, named the S@MoS_2(100) site.

Additionally, Bader charge analysis was performed on the MoS_2(100) and K/MoS_2(100) surfaces, with all results tabulated in Table 1. As presented in Table 1, the charge of distinct Mo sites on the MoS_2(100) surface falls within the range of +1.02 to +1.25$|e|$, while that of S sites ranges from −0.48 to −0.61$|e|$. After K atoms are loaded onto the MoS_2(100) surface, the negative charge of S sites adjacent to K increases to varying degrees due to the acceptance of additional electrons. In particular, the S3, S12, and S9 sites directly bonded to K exhibit a more pronounced charge shift. Based on the charge variation, it can be inferred that approximately 0.87$|e|$ of charge is transferred from K to the adjacent S sites. Moreover, the introduction of K induces a perturbation in the charge distribution of surface Mo sites. In comparison with Mo sites at the S edge, those located at the Mo edge experience a significant increase in charge following K loading.

CO activation

In CO hydrogenation with syngas, CO molecules first adsorb on the MoS_2 surface and then proceed through elementary steps, including direct dissociation or H-assisted activation, to generate various products. Therefore, elucidation the energetic, structural, and electronic characteristics of CO adsorbed on MoS_2 is essential for advancing the understanding of CO hydrogenation on MoS_2 catalysts and for facilitating the discovery of more efficient catalytic systems. A comprehensive

Table 2 Energy barriers and reaction energies of CO activation at different sites (E_a and $\Delta_r E$, eV)

		K-doped model				Pure model			
		Mo-edge		S-edge		Mo-edge		S-edge	
Label	Surface elementary steps	E_a	$\Delta_r E$	E_a	$\Delta_r E$	E_a	$\Delta_r E$	E_a	$\Delta_r E$
R1	CO + H → HCO	0.53	0.51	0.39	−0.44	1.19	0.03	0.52	−0.36
R2	CO + H → COH	0.80	0.77	1.67	−0.16	1.02	0.58	2.38	0.93

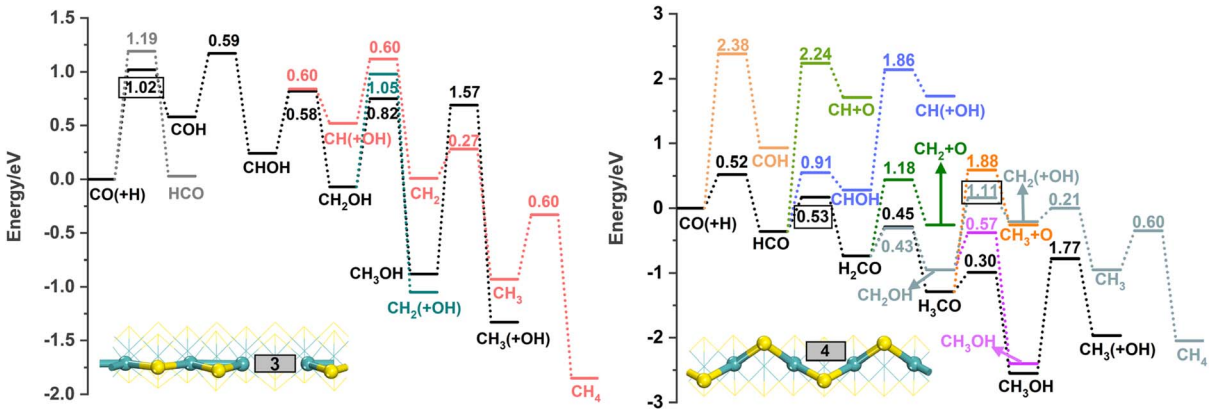

Fig. 5 Potential energy diagram of syngas conversion to C_1 products on Mo@MoS_2(100) site (left) and S@MoS_2(100) site (right).

investigation of all potential CO adsorption sites revealed that CO preferentially binds to the top site of the Mo atom with an adsorption energy of −2.68 eV. The adsorption energies at different sites are presented in Fig. S1 and S2. Notably, although the adsorption energy on the K atom is relatively weak (−0.58 eV, Fig. S3), CO can still adsorb at this site, suggesting that K doping structurally introduces additional sites for CO adsorption. The initial activation of CO may proceed *via* direct dissociation or through H-assisted formation of CHO or COH intermediates. Starting from adsorbed CO and H, all possible CO activation pathways were systematically explored at each site.

As shown in Fig. 3, the cyan curve corresponds to the hydrogenation of CO to form HCO, while the orange curve represents the hydrogenation step leading to COH formation on the Mo@MoS_2(100) site (solid line) and S@MoS_2(100) site (dashed line). At the Mo@MoS_2(100) site (solid line), CO adsorbed on the Mo atom can interact with H located on the adjacent S atom, with a C–H distance of 2.70 Å, thereby yielding HCO. In HCO structure, the C–H bond length is 1.11 Å. In the corresponding transition state, the C–H bond is elongated to 1.28 Å, with an energy barrier of 1.19 eV and an endothermicity of 0.03 eV. Alternatively, CO may react with the H atom adsorbed on the adjacent Mo–S to form COH, where the O–H bond decreases sequentially from 1.84 Å to 1.16 Å and finally to 0.99 Å. This step proceeds with an energy barrier of 1.02 eV and requires an endothermic input of 0.58 eV. Since the energy barrier for CO hydrogenation to COH (1.02 eV) is lower than that to HCO (1.19 eV), CO activation at this site predominantly yields COH species. At the S@MoS_2(100) site (dashed line), it is apparent that CO adsorbed on top of a Mo atom can couple with H co-adsorbed on the same Mo atom, with a C–H distance of 1.60 Å, leading to the formation of HCO. The C–H bond length in HCO is 0.98 Å. In the transition state, the C–H bond extends to 1.29 Å, with an associated energy barrier of 0.52 eV and an exothermicity of −0.36 eV. Alternatively, CO can react with H adsorbed on neighboring S atoms to generate COH, where the O–H bond distance decreases from 2.82 Å to 1.29 Å and finally to 1.11 Å. This pathway exhibits a much higher energy barrier of 2.38 eV and requires an endothermic input of 0.93 eV. Since the barrier for HCO formation (0.52 eV) is substantially lower, CO activation at this site is dominated by hydrogenation toward HCO species.

Similarly, a comprehensive transition state search was performed for the CO activation process on the K-doped MoS_2(100) surface model. The relevant results are summarized in Fig. 4. As

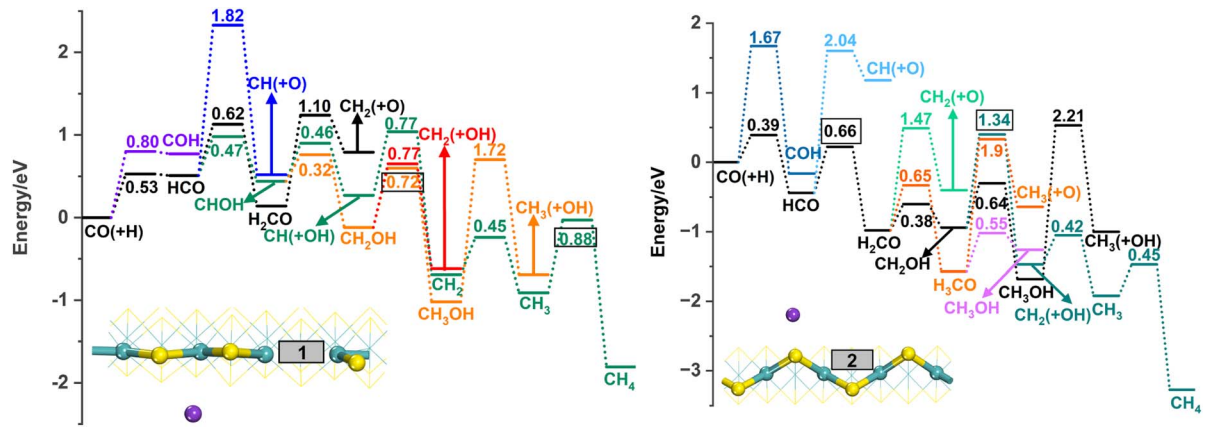

Fig. 6 Potential energy diagram of syngas conversion to C_1 products on Mo@K/MoS_2(100) site (left) and S@K/MoS_2(100) site (right).

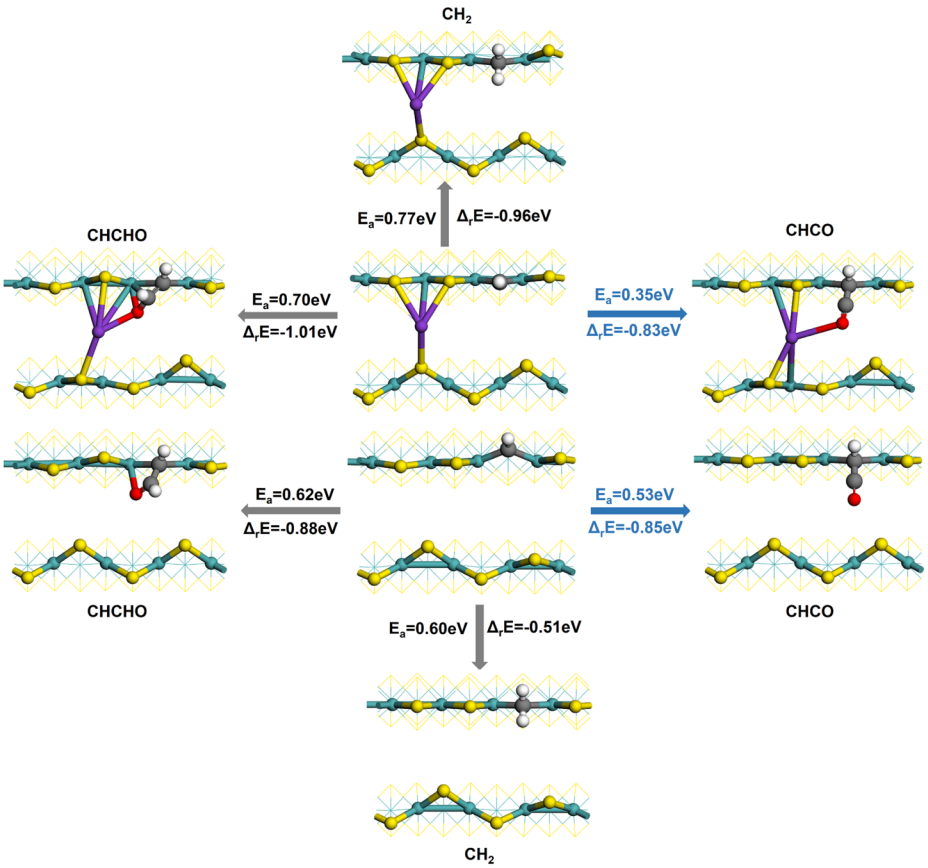

Fig. 7 Schematic diagram of the reaction behavior of CH species on the Mo@K/MoS_2(100) site (top) and Mo@MoS_2(100) site (bottom).

shown in Fig. 4, the blue pathway corresponds to the hydrogenation of CO to HCO, whereas the red pathway represents the hydrogenation of CO to COH at the same site. At the Mo@K/MoS_2(100) site (solid line), CO adsorbed on the Mo atom can interact with a neighboring H atom located on the S site, leading to the formation of a C–H bond. The bond distance decreases from the initial 1.67 Å to 0.98 Å in the final HCO product, with the transition state exhibiting a C–H bond length of 1.20 Å, an activation barrier of 0.53 eV, and an endothermic energy of 0.51 eV. Alternatively, CO may react with an H atom adsorbed on the adjacent Mo–S site to form COH. In this case, the O–H bond distance evolves from 2.66 Å to 1.14 Å and stabilizes at 1.12 Å, with a higher activation barrier of 0.80 eV and an endothermic energy of 0.77 eV. Importantly, the energy barrier for CO hydrogenation to COH (0.80 eV) exceeds that for CO hydrogenation to HCO (0.53 eV), suggesting that CO activation at this site preferentially proceeds through the formation of HCO species. At the S@K/MoS_2(100) site (dashed line), it is evident that CO adsorbed on a Mo atom can combine with an H atom, forming HCO with a C–H distance of 1.44 Å. The C–H bond length in the resulting HCO is 1.10 Å, and in the transition state extends to 1.16 Å, with an energy barrier of 0.39 eV and an exothermic release of −0.44 eV. Alternatively, CO can react with an H atom adsorbed on a neighboring S atom to produce COH, with the O–H bond distance transitioning from 2.68 Å to 1.64 Å and finally to 0.98 Å. This alternative process exhibits an energy barrier of 1.67 eV and an exothermic release of −0.16 eV. Notably, the significantly lower energy barrier for the hydrogenation of CO to HCO (0.39 eV) suggests that CO activation at this site primarily favors the formation of HCO species through hydrogenation.

In summary, both Mo-edge and S-edge sites are identified in this model. For CO activation on the K-doped MoS_2(100) surface, the reaction predominantly proceeds *via* hydrogen addition to the C atom, forming HCO species, regardless of the site type. In contrast, on the undoped MoS_2(100) surface, CO activation at the S-edge site mainly occurs through H to C forming HCO, whereas at the Mo-edge site it proceeds primarily through H addition to O, generating COH species. The differences in CO activation between the K-doped and undoped models are summarized in Table 2. The results show that on the K-doped MoS_2(100) surface, CO activation mainly follows the hydrogenation pathway leading to HCO formation. Comparison of the energy barriers at the two edge sites indicates that the S-edge exhibits higher activity. At the Mo-edge, the two activation pathways have comparable barriers, while at the S-edge the barrier for HCO formation is substantially lower than that for COH formation. A similar trend is observed for the undoped MoS_2(100) model. Furthermore, comparison of the same activation pathway between the two models reveals that K doping significantly reduces the CO activation barriers at each sites, independent of the reaction pathway. These results suggest that

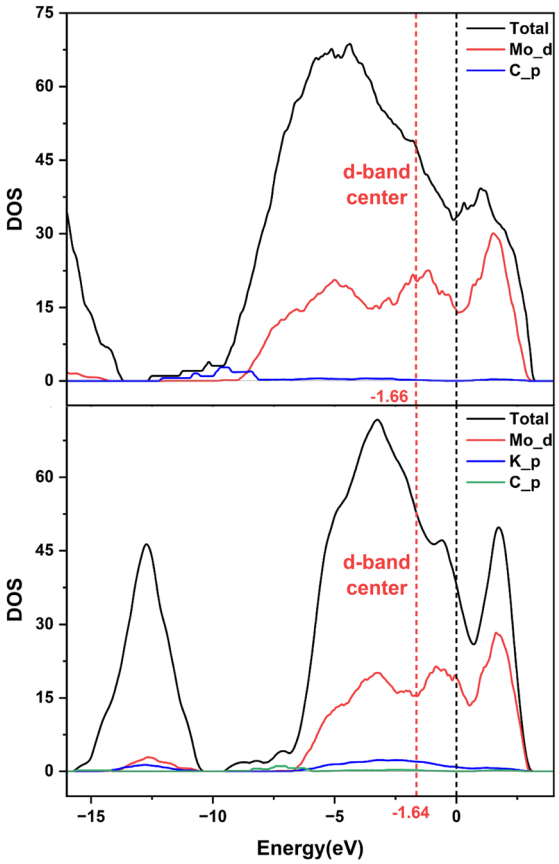

Fig. 8 Projected density of states of the adsorption structure of C_2 species on the Mo@MoS_2(100) (top) and Mo@K/MoS_2(100) (bottom).

K doping not only provides additional adsorption sites to facilitate CO adsorption but also renders CO activation more favorable.

Reaction pathways of C_1 intermediates formation

On the pure MoS_2(100) model, the conversion of syngas to C_1 products was systematically investigated at the Mo-edge site (left) and the S-edge site (right) in Fig. 5. At the Mo-edge site, the preferred pathway for methanol formation is CO → COH → CHOH → CH_2OH → CH_3OH, whereas methane formation proceeds through CO dissociation following the route CO → COH → CHOH → CH → CH_2 → CH_3 → CH_4. The energy barrier for CO activation at this site is 1.02 eV, representing the rate-limiting step of the overall process. Apart from this initial step, the CH_x species are mainly produced through stepwise hydrogenation of CH derived from CHOH cleavage. The energy barrier for CHOH cleavage is relatively low (0.60 eV), and subsequent hydrogenation of CH also proceeds with low barriers, enabling progressive hydrogenation to methane. In contrast, the final hydrogenation of CH_2OH in methanol formation exhibits a higher barrier of 0.82 eV, indicating that this site is more favorable for methane production. At the S-edge site, the optimal pathway for methanol formation is CO → HCO → H_2CO → H_3CO → CH_3OH, while the optimal pathway for methane formation is CO → HCO → H_2CO → CH_2OH → CH_2 → CH_3 → CH_4. In the methanol pathway, the most energy-demanding step is the hydrogenation of HCO to H_2CO, with a barrier of 0.53 eV. In the methane pathway, the cleavage of the C–O bond in CH_2OH to form CH_2 requires the highest barrier of 1.11 eV. These results suggest that methane is not the dominant product at this site, and only limited CH_x species are formed, with C_1 alcohols being the main products.

At the same time, the reaction pathways for syngas conversion to C_1 products on Mo-edge (left) and S-edge (right) sites of the K/MoS_2(100) model were also calculated, as shown in Fig. 6. On the Mo-edge site, the most favorable route for methanol formation is CO → HCO → CHOH → CH_2OH → CH_3OH, whereas that for methane formation is CO → HCO → CHOH → CH → CH_2 → CH_3 → CH_4. According to the data in Fig. 6, the highest energy barrier in the methanation pathway occurs in the final hydrogenation step (0.88 eV), while the highest barrier in methanol formation is also located at the last hydrogenation step (0.72 eV), which is lower than that of methanation. This indicates that methanol formation is more favorable at this site. Moreover, compared with the Mo-edge site of the MoS_2(100) surface, K doping significantly reduces the energy barrier for CO activation (0.53 eV), thereby enhancing the site reactivity. In addition, CH_x species are generated

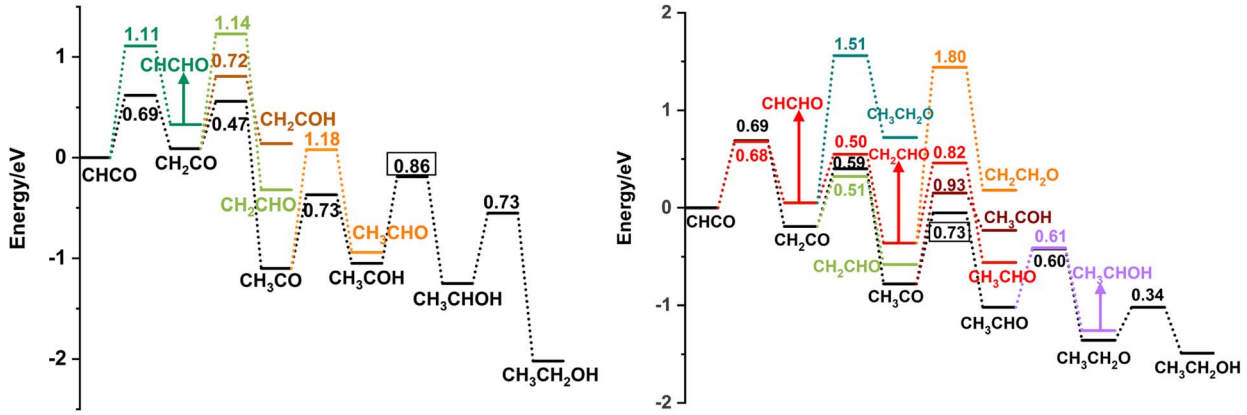

Fig. 9 Schematic diagram of the hydrogenation of CHCO species to ethanol on the Mo@MoS_2(100) (left) and Mo@K/MoS_2(100) (right).

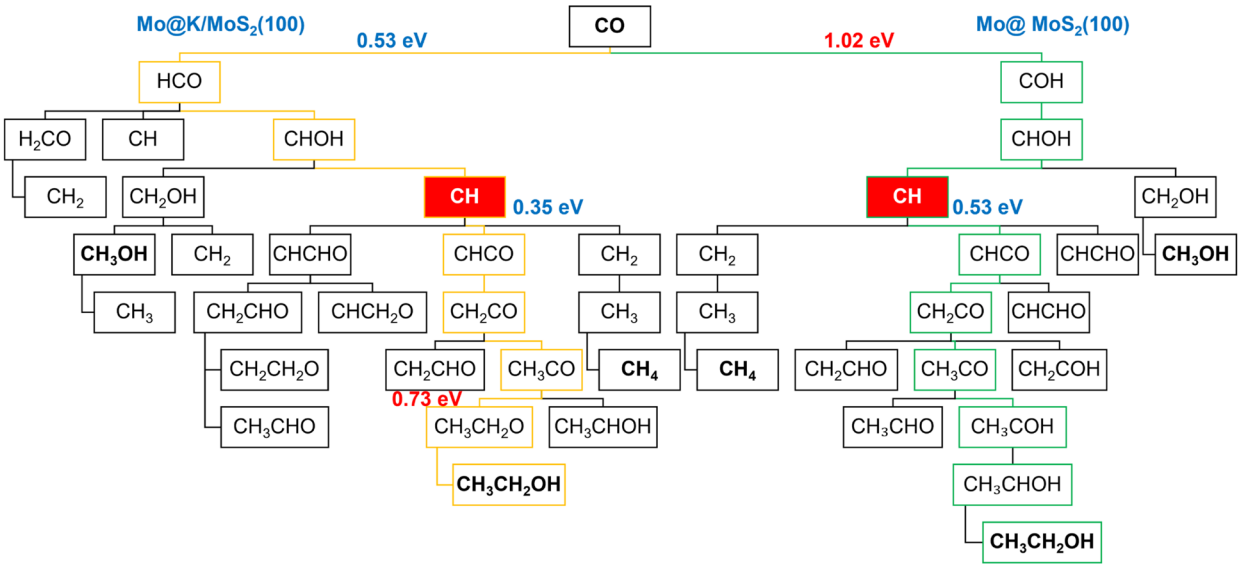

Fig. 10 Reaction network diagram of CO hydrogenation to ethanol on Mo@K/MoS_2(100) (left) and Mo@MoS_2(100) (right).

through stepwise hydrogenation after CHOH cleavage to CH. The energy barrier for CH formation is markedly lower than that at other sites, while subsequent hydrogenation of CH exhibits a considerably higher barrier. Consequently, CH is more likely to undergo coupling instead of methanation, suggesting that this site promotes chain growth toward higher alcohols. On the S-edge site, the methanol formation pathway is CO → HCO → H_2CO → CH_2OH → CH_3OH. The step with the highest barrier is the hydrogenation of HCO to H_2CO, with an energy barrier of 0.66 eV. Comparison with reported data indicates that methanol formation at this site is relatively feasible. The methane formation pathway is CO → HCO → H_2CO → CH_2OH → CH_2 → CH_3 → CH_4, where the rate-limiting step is the C–O bond cleavage of CH_2OH to form CH_2, with a barrier of 1.34 eV. These results suggest that methanol production is favored at this site, while methane is not the dominant product and CH_x intermediates are relatively scarce, making C_1 alcohol the main products.

C–C coupling

The formation of C_2 species proceeds *via* carbon–carbon coupling reactions. Previous density functional theory studies have shown that C–O bonds are readily cleaved at Mo-edge sites but remain stable at S-edge sites. Consequently, CH_x species are more likely to form at Mo-edge sites, with CH being the predominant intermediate. Since C–C coupling is a key step in ethanol formation, the reaction behavior of CH species at Mo-edge sites was examined for two models, including hydrogenation to form CH_2 and coupling with CO or HCO, as shown in Fig. 7. At the Mo@MoS_2(100) site, the energy barrier for CH hydrogenation to CH_2 is 0.60 eV with a reaction exotherm of −0.51 eV. The coupling of CH with CO to form CHCO has a barrier of 0.53 eV and an exotherm of −0.85 eV, whereas the coupling of CH with CHO to form CHCHO shows a barrier of 0.62 eV and an exotherm of −0.88 eV. Comparison of these pathways indicates that CH–CO coupling exhibits the lowest barrier at this site. At the Mo@K/MoS_2(100) site, the barrier for CH hydrogenation to CH_2 increases to 0.77 eV with an exotherm of −0.96 eV. In contrast, CH–CO coupling proceeds with a much lower barrier of 0.35 eV and an exotherm of −0.83 eV, while CH–CHO coupling requires 0.70 eV with an exotherm of −1.01 eV. Again, CH–CO coupling is the most favorable pathway. These results suggest that, regardless of K doping, C–C bond formation predominantly occurs through CH–CO coupling to yield CHCO species. Moreover, K doping substantially lowers the barrier for CH–CO coupling (0.35 eV compared with 0.53 eV without doping). This reduction is considered the primary reason for the enhanced alcohol selectivity observed upon K doping. To verify the stability of CHCO species adsorbed on the Mo@K/MoS_2(100) site under the typical 600 K reaction condition, additional *ab initio* molecular dynamics (AIMD) simulations were performed. As shown in Fig. S5, the adsorption configuration of CHCO exhibited almost no structural variation during the simulation process, demonstrating the high stability of this critical reaction intermediate at the experimental reaction temperature.

In addition, the projected density of states (PDOS) of the adsorption structures of C–C coupling products was calculated for both the K/MoS_2(100) site and the pristine MoS_2(100) surface. The PDOS diagram provides a means to determine whether two spatially adjacent atoms are bonded. As depicted in top of Fig. 8, the black curve represents the total DOS of the system, the red curve corresponds to the Mo_d orbital, and the blue curve corresponds to the C_p orbital. The Mo_d and C_p orbitals are spatially close, and the overlap between the red and blue curves at both adsorption sites confirms the presence of bonding between the C_2 species and the Mo atom. Meanwhile, as displayed in the bottom panel of Fig. 8, the red curve denotes the Mo_d orbital, while the blue curve represents the K_p orbital. The Mo d- and K p-orbitals are also spatially proximal,

and the distinct overlap of the two curves at the two adsorption sites verifies the formation of bonding interactions between K and Mo atoms.

Furthermore, PDOS analysis can be applied to the d-band center theory. This theory states that for transition-metal-based catalysts, the energy band associated with the d orbital is defined as the d-band, and the position of its center relative to the Fermi level predicts catalytic reactivity. A d-band center closer to the Fermi level indicates enhanced catalytic activity. As illustrated in Fig. 8, after K doping, the d-band center of Mo shifts significantly toward the Fermi level, suggesting that the electronic states of the MoS_2-based catalyst exhibit higher chemical activity, thereby strengthening the interaction between reactants and the catalyst and accelerating the reaction process.

Post C–C coupling steps leading to C_2 oxygenates

Based on the previous calculations, the subsequent hydrogenation of CHCO species leading to ethanol formation was further examined, as shown in Fig. 9. On the Mo-edge site of the K/MoS_2(100) model (right), the optimal pathway proceeds as CHCO → CH_2CO → CH_3CO → CH_3CHO → CH_3CH_2O → CH_3CH_2OH. The data indicate that the hydrogenation of CH_3CO to CH_3CHO, with an energy barrier of 0.73 eV, is the most energy-demanding step. This step is therefore identified as the rate-determining step on this site. For comparison, the hydrogenation of CHCO species on the Mo-edge site of the undoped MoS_2(100) model (left) was also calculated, and the results are shown in Fig. 9 (left). In this case, the preferred pathway is CHCO → CH_2CO → CH_3CO → CH_3COH → CH_3CHOH → CH_3CH_2OH. The highest energy barrier in this sequence corresponds to the hydrogenation of CH_3COH to CH_3CHOH, with a value of 0.86 eV. Considering the preceding CH species formation process, the most feasible overall pathway for syngas conversion to ethanol on this surface is CO → COH → CHOH → CH → CHCO → CH_2CO → CH_3CO → CH_3CHO → CH_3CH_2O → CH_3CH_2OH. Among these steps, the activation of CO to COH, with an energy barrier of 1.02 eV, is the most difficult and serves as the rate-determining step. Notably, this barrier is much higher than that of the rate-determining step on the K-doped model, which accounts for the experimentally observed significant enhancement in alcohol selectivity after K doping.

Reaction network

Based on the above discussion, a relatively complete reaction network for the conversion of syngas to C_2 species on the MoS_2(100) surface was established, as shown in Fig. 10. The calculations reveal that CO hydrogenation to mixed alcohols on MoS_2(100) surface is a highly complex process that can yield multiple products, with all hydrogenation products competing through different formation pathways. Consequently, clarifying the reaction network of syngas conversion is essential for evaluating product selectivity and yield. The results further indicate that CO conversion proceeds differently at different reaction sites. On MoS_2(100) surface, CH is the key intermediate, and its reaction behavior determines whether alcohols are produced. K doping promotes both CO activation and C–C coupling. The optimal pathway for ethanol formation changes upon K doping. For the K-doped catalyst, the pathway shown on the left side of Fig. 10 proceeds through the hydrogenation of CH_3CO to CH_3CHO as the key step. In contrast, for the undoped catalyst, the pathway depicted on the right side of Fig. 10 proceeds with CO activation as the critical step.

Conclusions

We systematically investigated the catalytic mechanism of CO hydrogenation to ethanol on MoS_2(100) surfaces before and after K-doping using density functional theory, providing a comprehensive evaluation of the promoter effect. The main results are summarized as follows:

(1) On the Mo-edge of pristine MoS_2(100), methane formation is favored, whereas the Mo-edge of K/MoS_2(100) promotes methanol production. The high energy barrier for CO activation on the Mo-edge of pristine MoS_2(100) leads to low activity, which is markedly enhanced upon K-doping.

(2) Both pristine and K-doped K/MoS_2(100) S-edges favor methanol generation. However, the cleavage of the C–O bond to form CH_x species involves high barriers at these sites, resulting in C_1 alcohols as the dominant products.

(3) Ethanol formation proceeds through the coupling of CH_x and CH_yO intermediates. CH_x species, mainly CH, are readily produced at Mo-edge sites. CH faces three options: hydrogenation to form CH_2, coupling with CO or CHO, with the last pathway being more favorable due to a lower energy barrier. K-doping substantially reduces this barrier, thereby facilitating ethanol synthesis.

(4) On the Mo-edge of K/MoS_2(100), the most favorable pathway for ethanol formation from syngas is: CO → HCO → CHOH → CH → CHCO → CH_2CO → CH_3CO → CH_3CHO → CH_3CH_2O → CH_3CH_2OH. The rate-determining step is the hydrogenation of CH_3CO to CH_3CHO, with a barrier of 0.73 eV.

(5) For pristine MoS_2(100) on the Mo-edge, a similar route is observed, but the highest barrier corresponds to CO activation to COH (1.02 eV).

Author contributions

Yaru Dang: investigation, data curation, formal analysis, investigation, methodology, visualization, writing – review & editing. Qianji Han: investigation, writing – original draft preparation. Ruihan Wang: data analysis. Ziyan Wei: visualization, investigation. Meng Wang: methodology, conceptualization. Bin Qin: supervision, writing – review & editing.

Conflicts of interest

The authors declare no conflict of interest.

Data availability

The data that support the findings of this study are available from the corresponding author upon reasonable request.

Supplementary information (SI) is available. See DOI: https://doi.org/10.1039/d5ra08871b.

Acknowledgements

This work was supported by the Provincial Basic Scientific Research Fund Special Project of Hebei University of Science and Technology Normal College (2023JK03), the Science Research Project of Hebei Education Department (BJK2023019) and the Hebei Natural Science Foundation (B2023407004). We gratefully acknowledge HZWTECH for providing computation facilities.

References

1 S. Han, D. Fan, N. Chen, W. Cui, L. He, P. Tian and Z. Liu, *ACS Catal.*, 2023, **13**, 10651–10660.
2 J. Xiao, H. Meng, C. Wang and F. Xiao, *ChemCatChem*, 2025, **17**, 202401731.
3 W. Zhao, Z. Chang, M. Fan, B. Wang and R. Zhang, *Fuel*, 2023, **342**, 127858.
4 H. Shen, K. Liu, J. Li, R. Zhang, K. Gong, Y. An, T. Lin and L. Zhong, *ACS Catal.*, 2025, **15**, 6173–6185.
5 Z. Li, G. Luo, X. Pei, C. Gao, J. Lv, S. Huang, Y. Wang and X. Ma, *ACS Catal.*, 2025, **15**, 4069–4080.
6 A. E. Farrell, R. J. Plevin, B. T. Turner, A. D. Jones, M. O'Hare and D. M. Kammen, *Science*, 2006, **311**, 506–508.
7 G. Liu, G. Yang, X. Peng, J. Wu and N. Tsubaki, *Chem. Soc. Rev.*, 2022, **51**, 5606–5659.
8 A. J. Ragauskas, C. K. Williams, B. H. Davison, G. Britovsek, J. Cairney, C. A. Eckert, W. J. Frederick, J. P. Hallett, D. J. Leak and C. L. Liotta, *Science*, 2006, **311**, 484–489.
9 H. T. Luk, C. Mondelli, D. C. Ferré, J. A. Stewart and J. Pérez-Ramírez, *Chem. Soc. Rev.*, 2017, **46**, 1358–1426.
10 C. Chen, M. Garedew and S. W. Sheehan, *Nat. Chem.*, 2024, **16**, 1566.
11 W. Zhou, S. R. Docherty, E. Lam, C. Ehinger, X. Zhou, Y. Hou, P. Laveille and C. Copéret, *J. Am. Chem. Soc.*, 2025, **147**, 12890–12896.
12 C. Wang, J. Zhang, G. Qin, L. Wang, E. Zuidema, Q. Yang, S. Dang, C. Yang, J. Xiao, X. Meng, C. Mesters and F. Xiao, *Chem*, 2020, **6**, 646–657.
13 J. J. Spivey and A. Egbebi, *Chem. Soc. Rev.*, 2007, **36**, 1514–1528.
14 Y. Sheng, M. V. Polynski, M. K. Eswaran, B. Zhang, A. M. H. Lim, L. Zhang, J. Jiang, W. Liu and S. M. Kozlov, *Appl. Catal., B*, 2024, **343**, 123550.
15 J. Hu, Z. Wei, Y. Zhang, R. Huang, M. Zhang, K. Cheng, Q. Zhang, Y. Qi, Y. Li, J. Mao, J. Zhu, L. Wu, W. Wen, S. Yu, Y. Pan, J. Yang, X. Wei, L. Jiang, R. Si, L. Yu, Y. Wang and D. Deng, *Nat. Commun.*, 2023, **14**, 6808.
16 J. R. Rostrup-Nielsen, *Chem. Rev.*, 2004, **46**, 247–270.
17 G. W. Huber, S. Iborra and A. Corma, *Chem. Rev.*, 2006, **106**, 4044–4098.
18 R. G. Herman, *Catal. Today*, 2000, **55**, 233–245.
19 S. Lee and A. Sardesai, *Top. Catal.*, 2005, **32**, 197–207.
20 M. Ao, G. H. Pham, J. Sunarso, M. O. Tade and S. Liu, *ACS Catal.*, 2018, **8**, 7025–7050.
21 Y. Li, L. Zhao, X. Liu, C. Zeng and K. Fang, *J. Fuel Chem. Technol.*, 2019, **47**, 513–521.
22 M. T. Claure, S. H. Chai, S. Dai, K. A. Unocic, F. M. Alamgir, P. K. Agrawal and C. W. Jones, *J. Catal.*, 2015, **324**, 88–97.
23 E. Mahmoudi, A. Sayyah, S. Farhoudi, Z. Bahranifard, G. Behmenyar, A. Z. Turan, N. Delibas and A. Niaei, *J. CO_2 Util.*, 2024, **86**, 102893.
24 T. Gu, B. Wang, S. Chen and B. Yang, *ACS Catal.*, 2020, **10**, 6346–6355.
25 N. Koizumi, G. Z. Bian, K. Murai, T. Ozaki and M. Yamada, *J. Mol. Catal. A: Chem.*, 2004, **207**, 173–182.
26 A. K. Gunturu, E. L. Kugler, J. B. Cropley and D. B. Dadyburjor, *Ind. Eng. Chem. Res.*, 1998, **37**, 2107–2115.
27 E. Bertheussen, A. Verdaguer-Casadevall, D. Ravasio, J. H. Montoya, D. B. Trimarco, C. Roy, S. Meier, J. Wendland, J. K. Nørskov, I. E. L. Stephens and I. Chorkendorff, *Angew. Chem.*, 2016, **128**, 1472–1476.
28 L. Wang, B. Bai, H. Bai, Y. Duan, M. Yang, Z. Wei, Z. Zuo, J. Zuo and W. Huang, *Fuel*, 2023, **349**, 128506.
29 J. Chen, Z. Wang, J. Zhao, L. Ling, R. Zhang and B. Wang, *Appl. Surf. Sci.*, 2021, **540**, 148301.
30 J. Hu, Y. Wang, C. Cao, D. C. Elliott, D. J. Stevens and J. F. White, *Catal. Today*, 2007, **120**, 90–95.
31 P. E. Blöchl, *Phys. Rev. B: Condens. Matter Mater. Phys.*, 1994, **50**, 17953–17979.
32 G. Kresse and J. Hafner, *Phys. Rev. B: Condens. Matter Mater. Phys.*, 1993, **47**, 558–561.
33 G. Kresse and J. Furthmüller, *Phys. Rev. B: Condens. Matter Mater. Phys.*, 1996, **54**, 11169.
34 J. P. Perdew, K. Burke and M. Ernzerhof, *Phys. Rev. Lett.*, 1996, **77**, 3865.
35 H. Tominaga, Y. Aoki and M. Nagai, *Appl. Catal., A*, 2012, **423**, 192–204.
36 H. J. Monkhorst and J. D. Pack, *Phys. Rev. B*, 1976, **13**, 5188.
37 G. Henkelman and H. Jónsson, *J. Chem. Phys.*, 2000, **113**, 9978–9985.
38 G. Henkelman, B. Uberuaga and H. Jonsson, *J. Chem. Phys.*, 2000, **113**, 9901–9904.
39 P. E. Blöchl, *Phys. Rev. B: Condens. Matter Mater. Phys.*, 1994, **50**, 17953.
40 W. Hoover, *Phys. Rev. A: At., Mol., Opt. Phys.*, 1985, **31**, 1695–1697.
41 S. Nosé, *J. Chem. Phys.*, 1984, **81**, 511–519.
42 S. Thomas, S. Moolayadukkam and K. P. Priyanka, *Science and Technology of 2D MoS_2*, 2024, pp. 55–64.
43 P. Joensen, E. D. Crozier, N. Alberding and R. F. Frindt, *J. Phys. C: Solid State Phys.*, 1987, **20**, 4043.
44 A. Andersen, S. M. Kathmann, M. A. Lilga, K. O. Albrecht, R. T. Hallen and D. Mei, *Catal. Commun.*, 2014, **52**, 92–97.
45 L. Lemeur, D. Dupont, C. Raybaud and J. Daudin, *J. Catal.*, 2011, **279**, 276–286.